Fourier transform imaging spectroscopy with a multiple-aperture telescope: band-by-band image reconstruction

Samuel T. Thurman* and James R. Fienup
The Institute of Optics, University of Rochester, Rochester, NY 14627

ABSTRACT

Fourier transform imaging spectroscopy can be performed with a segmented-aperture telescope or a multiple-telescope array using the subaperture piston control mechanisms. Spectrum recovery from intensity measurements is analyzed for a general aperture configuration. The spatial transfer functions of the recovered spectral images are shown to vanish necessarily at the DC spatial frequency. This poses an interesting image reconstruction problem as the recovered spectral data is missing low spatial-frequency content. Results of a band-by-band reconstruction of simulated data are presented where the low spatial frequency data is reconstructed by maximizing a sharpness metric based on the spatial derivatives of the object estimate.

Keywords: Fourier transform spectroscopy, segmented-aperture telescopes, multiple-telescope array, physical optics, image reconstruction

1. INTRODUCTION

Segmented-aperture telescopes and multiple-telescope arrays (MTA's) are systems that use a collection of relatively small aperture optics to achieve a resolution equivalent to a larger-aperture monolithic system. In a segmented-aperture system, the primary is sectioned, while in a multiple-telescope system, light is collected by an array of telescopes and imaged to a common plane. Resolutions higher than that of an individual subaperture (one section of the primary or a single telescope from the array) can only be achieved if the optical path lengths through each subaperture are equal. Thus, such systems have independent optical path-length or piston control mechanisms for each subaperture. While this article concentrates on multiple-telescope arrays, the techniques described apply equally to segmented-aperture systems. Figure 1 is an illustration of a MTA having only two subapertures, in which the piston control/path delay mechanisms are shown as movable corner mirrors. Such systems offer some advantages over comparable monolithic systems, including reduced weight and volume,[1] and reduced cost.[2] One of the more important technical challenges involved with using a segmented-aperture or multiple-telescope system is the phasing of the subapertures. The phase diversity technique is one way to accomplish this with the addition of only a beamsplitter and an extra detector to the system.[3,4]

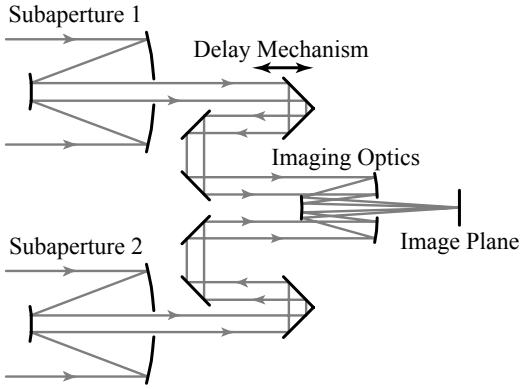

Figure 1. Illustration of a multiple-telescope array having only two subapertures.

* thurman@optics.rochester.edu; phone 1 585 275-8008; optics.rochester.edu

Fourier transform spectroscopy is a well-established technique for obtaining spectral information from a series of polychromatic intensity measurements.[5] Typically, Fourier transform imaging spectroscopy (FTIS) is performed by relaying an image through a Michelson interferometer,[6] making a series of intensity measurements with various optical path differences (OPD's) between the arms of the interferometer, and recovering the spectral data through post-processing. In an MTA, the existing path delay lines can be used to introduce the OPD's required for the spectroscopy. Such an implementation is an alternative to the addition of a Michelson interferometer at the back end of the telescope. Kendrick *et al.*[7] demonstrated this technique for a two-aperture system imaging an array of point sources. Here, we show that the spatial transfer functions for the spectral images from such a system are zero-valued in some finite region about the DC spatial frequency,[8] which makes imaging extended objects more difficult. This presents an interesting image reconstruction problem, as the spectral images are missing low spatial frequency information. We present a nonlinear sharpness metric, based on the spatial derivatives of the object estimate, and use this metric to reconstruct the missing low spatial frequency content of simulated FTIS data from an MTA. Here, the data is reconstructed independently for each spectral band.

Section 2 presents the basic theory for modeling the intensity measurements in a segmented-aperture telescope or MTA, the post-processing steps needed to recover spectral data from the intensity measurements, some noise considerations, and the image reconstruction algorithm. Section 3 presents results for a simulation of a six-aperture MTA, including a band-by-band reconstruction of the FTIS data. Section 4 is a discussion of the simulation results.

2. THEORY

2.1. Measurements

The modeling is based on the simplified refractive system shown in Figure 2. This system contains: (i) an object plane with spatial coordinates (x_o, y_o), (ii) a collimating lens with focal length f_o, (iii) a pupil plane, with spatial coordinates (ξ,η), containing the subapertures and corresponding path-delay elements of the telescope, (iv) an imaging lens with focal length f_i, and (v) an image plane with spatial coordinates (x,y). The object is assumed to be polychromatic and spatially incoherent with a spectral density $S_o(x_o,y_o,\nu)$, where ν is the optical frequency. The magnification of the system is $M = -f_i/f_o$. In general there may be any number of subapertures, of which the path-delays can be controlled independently. Here, we only consider the case where the subapertures are divided into two groups: during the measurements the subapertures in the first group have zero path delay, while those in the second have a common path delay. The scalar field transmission functions in the pupil plane for the for each group of subapertures are written as $T_1(\xi,\eta)$ and $T_2(\xi,\eta)$, respectively, where the system is assumed to be aberration-free and the effect of the path delay elements are left out of the transmission functions by definition. The path delay for the second group of subapertures is written as $c\tau$, where c is the speed of light and τ is an equivalent time delay variable.

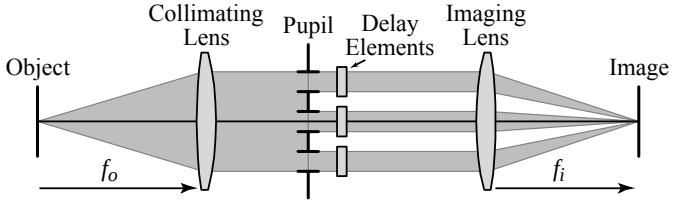

Figure 2. Simplified refractive model of a segmented-aperture or multiple-telescope system.

Making paraxial approximations,[9] the image intensity $I(x,y,\tau)$ is given by the standard incoherent imaging equation for polychromatic light, *i.e.*,

$$I(x_i, y_i, \tau) = \kappa \int_{-\infty}^{\infty}\int_{-\infty}^{\infty}\int_{-\infty}^{\infty} \frac{1}{M^2} S_o\left(\frac{x'}{M}, \frac{y'}{M}, \nu\right) h(x_i - x', y_i - y', \nu, \tau)\, dx'dy'd\nu \,, \tag{1}$$

where the image intensity is written explicitly as a function of the time delay variable, $\kappa = \lambda^2/\pi$ for a perfectly incoherent object, $x' = Mx_o$, $y' = My_o$, and $h(x_i,y_i,\nu,\tau)$ is the normalized monochromatic point spread function (PSF) of the optical system, which can be written as

$$h(x_i,y_i,\nu,\tau) = h_{1,1}(x_i,y_i,\nu) + h_{1,2}(x_i,y_i,\nu)\exp(-i2\pi\nu\tau) + h_{2,1}(x_i,y_i,\nu)\exp(i2\pi\nu\tau) + h_{2,2}(x_i,y_i,\nu), \tag{2}$$

where the terms $h_{p,q}(x_i,y_i,\nu)$ are referred to as spectral point spread functions (SPSF's) and defined as

$$h_{p,q}(x_i,y_i,\nu) = t_p(x_i,y_i)\,t_q^*(x_i,y_i), \tag{3}$$

where

$$t_p(x_i,y_i) = \frac{1}{\lambda^2 f_i^2}\int_{-\infty}^{\infty}\int_{-\infty}^{\infty} T_p(\xi,\eta)\exp\left[-i2\pi\left(\frac{x_i}{\lambda f_i}\xi + \frac{y_i}{\lambda f_i}\eta\right)\right]d\xi d\eta \tag{4}$$

is the coherent impulse response for the pth subaperture group.

For FTIS, the image intensity is measured over a range of time delays τ. The measured data set, which has two spatial coordinates and a time-delay coordinate, will be referred to as the raw data cube. The data in this cube represents a measured fringe packet along the τ-dimension at each spatial coordinate (x_i,y_i).

2.2. Spectral data

Spectral data is recovered from the raw data cube by the standard Fourier technique: (i) subtracting the bias from the fringe packet at each point in the image plane, and (ii) Fourier transforming the τ-dimension to ν'. Starting from Eq. (1) and using an infinite continuous Fourier transform, the spectral image can be written as

$$\begin{aligned} S_i(x_i,y_i,\nu') = {} & \kappa\int_{-\infty}^{\infty}\int_{-\infty}^{\infty}\frac{1}{M^2}S_o\left(\frac{x'}{M},\frac{y'}{M},-\nu'\right)h_{1,2}(x_i-x',y_i-y',-\nu')\,dx'dy' \\ & + \kappa\int_{-\infty}^{\infty}\int_{-\infty}^{\infty}\frac{1}{M^2}S_o\left(\frac{x'}{M},\frac{y'}{M},\nu'\right)h_{2,1}(x_i-x',y_i-y',\nu')\,dx'dy'. \end{aligned} \tag{5}$$

Note that this equation represents a set of spectral images given by a magnified version of the object spectral density convolved spatially with the SPSF's at each optical frequency. By definition, the object spectral density is real-valued, non negative, and non-zero only for positive frequencies. However, the quantity in Eq. (5) can be non-zero for negative frequencies, and the definition of the SPSF's [see Eq. (3)] implies that the spectral data is complex-valued in general. Since the intensity measurements are real-valued, the spectral data possesses Hermitian symmetry about $\nu' = 0$: $S_i(x,y,-\nu') = S_i^*(x,y,\nu')$. $S_i(x,y,\nu')$ can be referred to as the complex-valued spectral image cube.

Transforming the spectral image cube into the spatial frequency domain yields

$$G_i(f_x,f_y,\nu') = \kappa\left[G_o(Mf_x,Mf_y,-\nu')H_{1,2}(f_x,f_x,-\nu') + G_o(Mf_x,Mf_y,\nu')H_{2,1}(f_x,f_y,\nu')\right], \tag{6}$$

where $G_i(f_x,f_y,\nu')$ and $G_o(f_x,f_y,\nu')$ are the two-dimensional spatial Fourier transforms of $S_i(x,y,\nu')$ and $S_o(x,y,\nu')$, respectively, and the terms $H_{p,q}(f_x,f_y,\nu')$ are spectral optical transfer functions (SOTF's) defined as

$$H_{p,q}(f_x,f_y,\nu') = \frac{T_p(-\lambda f_i f_x,-\lambda f_i f_y)\star T_q(-\lambda f_i f_x,-\lambda f_i f_y)}{\int_{-\infty}^{\infty}\int_{-\infty}^{\infty}\sum_{p=1}^{Q}|T_p(\xi,\eta)|^2\,d\xi d\eta}, \tag{7}$$

where $\star$ represents a two-dimensional cross-correlation with respect to the spatial frequency variables. Note that the SOTF's in Eq. (7) are given by the cross-correlations of the two subaperture groups. Furthermore, the SOTF's vanish

necessarily at the DC spatial frequency, since the subapertures are physically non-overlapping in the pupil plane. In an actual system, there will be a minimum distance between subapertures, and the SOTF's will vanish in some finite region around DC. Thus, the DC and some low spatial-frequency components will be missing from the FTIS data. $G_i(f_x,f_y,\nu')$ is referred to as the spectral/spatial-frequency cube.

2.3. Noise

In a real system, the intensity measurements are sampled, there is noise in the measurements, and discrete Fourier transforms (DFT's) are used instead of continuous transforms. While the noise may come from various sources, usually it is assumed that the noise includes both Poisson (photon) noise and Gaussian detector noise. Even if the noise in the measurements is dominated by Poisson noise, the noise in the real and imaginary parts of the complex-valued spectral images is spatially independent and Gaussian since it is a linear combination of many random variables (through the DFT operation). In general, the noise in the spectral images is spatially non-uniform due to the Poisson noise component in the measured data. The noise in the spectral/spatial-frequency cube is Gaussian, nearly uncorrelated, and approximately uniform in the spatial frequency dimensions.

2.4. Band-by-band image reconstruction

The FTIS images obtained from a segmented-aperture telescope or MTA require a nonlinear image reconstruction algorithm, since low spatial frequency information is missing from the data. Linear algorithms, such as the Wiener-Helstrom filter,[10] can only restore measured spatial frequencies, *i.e.*, where the SOTF's terms are non-zero, while nonlinear algorithms offer the ability to fill-in missing data based on various assumptions about the object. Here, we describe a nonlinear algorithm that we used for band-by-band reconstructions of simulated FTIS data in Sec. 3.

Our approach is to formulate the image reconstruction problem as a constrained optimization, in which an objective function is minimized or maximized subject to constraints that ensure that the solution is consistent with the measured data and prior information. Example objective functions include entropy,[11] maximum likelihood,[12,13] and various sharpness metrics.[14,15] We have had success filling-in missing low spatial frequencies by maximizing the following derivative-based sharpness metric

$$E_l = \frac{1}{MN}\sum_{m=1}^{M}\sum_{n=1}^{N}\exp\left\{\frac{-1}{2\sigma_g^2}\left[g_{est}(m,n,l)-g_{est}(m+1,n,l)\right]^2\right\}+\exp\left\{\frac{-1}{2\sigma_g^2}\left[g_{est}(m,n,l)-g_{est}(m,n+1,l)\right]^2\right\}, \quad (8)$$

where $g_{est}(m,n,l)$ represents a discrete estimate of the object spectral density, the integers $m \in [1,M]$ and $n \in [1,N]$ are spatial samples in the x- and y-directions, l is a particular spectral sample, and σ_g is a normalization constant. This metric is related to Muller and Buffington's[14] sharpness metric S_4 in that it is based on the spatial derivatives of the object estimate. Note that individual terms in the summation are maximized when the finite-difference derivatives of the object estimate in the x- or the y-directions are zero, or at least small compared to σ_g. Thus, the maximization of this metric implies a particular assumption about the scene, *i.e.*, the scene consists of regions that are spatially uniform. We find that this metric changes with respect to the derivative (finite difference) values most rapidly when the magnitude of the derivative is near σ_g. Hence, the metric puts most emphasis on reducing these derivatives and cares less about very large magnitude derivatives.

To formulate a data-consistency constraint, we let $G_{est}(u,v,l)$ represent the two-dimensional spatial DFT of $g_{est}(m,n,l)$, where $u \in [1,M]$ and $v \in [1,N]$ are spatial frequency samples in the f_x- and f_y-directions. Then, we define the following constraint function for each spectral band

$$C_l = 1-\frac{1}{2K}\sum_{\substack{u=1\\ H_{2,1}(u,v,l)\neq 0}}^{M}\sum_{v=1}^{N}\frac{\left|H_{2,1}(u,v,l)G_{est}(u,v,l)-G_i(u,v,l)\right|^2}{\sigma^2}, \quad (9)$$

where $H_{2,1}(u,v,l)$ is a discrete version of the SOTF $H_{2,1}(f_x,f_y,\nu')$, $G_i(u,v,l)$ are the measured samples of the spectral/spatial-frequency cube, σ^2 is the variance of the noise in the real and imaginary parts of the spectral/spatial-frequency cube, and K is the number of spatial frequency components for which $H_{2,1}(u,v,l)$ is non-zero. Note that we are only

reconstructing the data for positive frequencies ($\nu' > 0$), and therefore Eq. (9) only contains the SOTF term $H_{2,1}(f_x,f_y,\nu')$ and not $H_{1,2}(f_x,f_y,\nu')$. Also, note that for $C_l \geq 0$, $G_{est}(u,v,l)$ agrees on average with the measured spatial frequency data to within the standard deviation of the noise. Thus, the agreement between the reconstruction and the measurements is reasonable when the constraint is satisfied. In the context of the optimization problem, the constraint $C_l \geq 0$ defines a set of feasible solutions over which a chosen metric is to be minimized or maximized. In practice, we solve the constrained optimization problem by incorporating the constraint into a sequence of new objective functions as a quadratic penalty function,[16] which are solved by a conjugate-gradient[17,18] routine with analytically calculated gradients.

Note that the FTIS data does not contain band-by-band information about the DC components of the spectral images, and a band-by-band reconstruction using the metric in Eq. (8) and constraint in Eq. (9) will not yield meaningful DC components. Here, after such a reconstruction we add DC components to make the reconstructed spectral images non negative on a band-by-band basis, since the object spectral density must be non negative. This is done, for each l, by subtracting the minimum of $g_{est}(m,n,l)$ from $g_{est}(m,n,l)$.

3. SIMULATION

The telescope modeled for the simulation contains six circular subapertures arranged in a hexagonal pattern, as shown in Figure 3(a). The subapertures are divided into two groups, one group that has zero path-delay and the other group has a common path-delay. The figure shows which subapertures belong to each group. Note that the SOTF terms scale with the optical frequency. Figure 3(b) and 3(c) show the SOTF's for the largest optical frequency used in the simulations. Note there is area around DC where the amplitude of the SOTF's is zero or small. This corresponds to the range of spatial frequencies around DC where the FTIS data will be missing or highly attenuated.

The scene used for the simulation is shown in Figure 4. The scene is composed of the sum of two uniform rectangular objects, with different spectral densities, embedded in a dark background. The spectral data is limited to optical wavelengths from 400 to 700 nm, or from 430 to 750 THz in frequency units. Simulated intensity measurements in units of photons are shown in Figure 5. The interference fringes are oversampled by 20% with OPD increments of $c\Delta\tau$ = 167 nm over a range of $-10.67\ \mu m < c\tau \leq 10.67\ \mu m$ with 128 samples. The resulting spectral resolution in the FTIS data is $\Delta\nu$ = 14.1 THz, or 469 cm^{-1} in wavenumber units, or $\Delta\lambda$ = 14 nm at λ = 550 nm in terms of wavelength. The magnitude of the measurements is scaled such that the average number of photons per pixel with zero path delay ($\tau = 0$) is 10,000. The only noise included in the simulated measurements is photon noise.

Complex-valued spectral images are obtained from the intensity measurements by Fourier transforming from the τ-domain to the ν'-domain. Figure 6(a) shows the real part of one such spectral image. Notice that the image is zero-mean since the DC component is missing. The low spatial frequency content of the rectangular objects is missing also, but the image contains edge information. Figure 6(b) shows a Wiener-Helstrom reconstruction of the spectral image. The Wiener filter has sharpened the edges considerably and filtered out some of the noise, but cannot fill in the missing

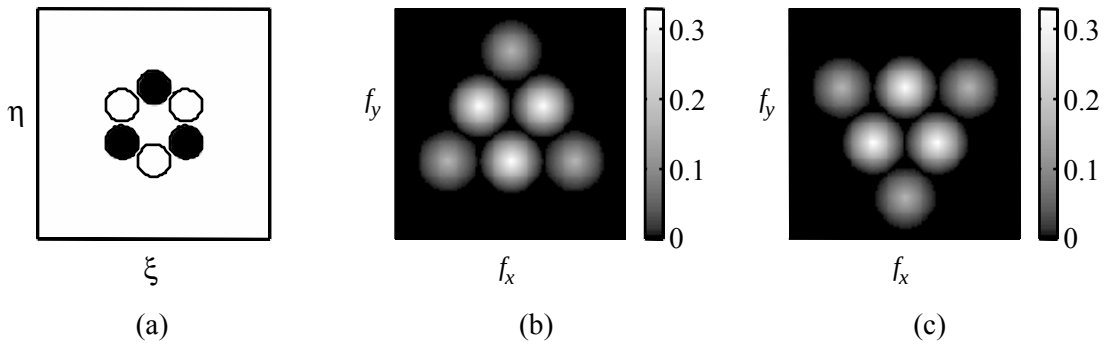

Figure 3. Telescope configuration used for simulations: (a) pupil configuration (subapertures with zero path-delay are shown in black, and those with a common path-delay are shown in white), (b) SOTF term $H_{1,2}(f_x,f_y,\nu')$ for FTIS data at $\nu' < 0$, and (c) SOTF term $H_{2,1}(f_x,f_y,\nu')$ for FTIS data at $\nu' > 0$.

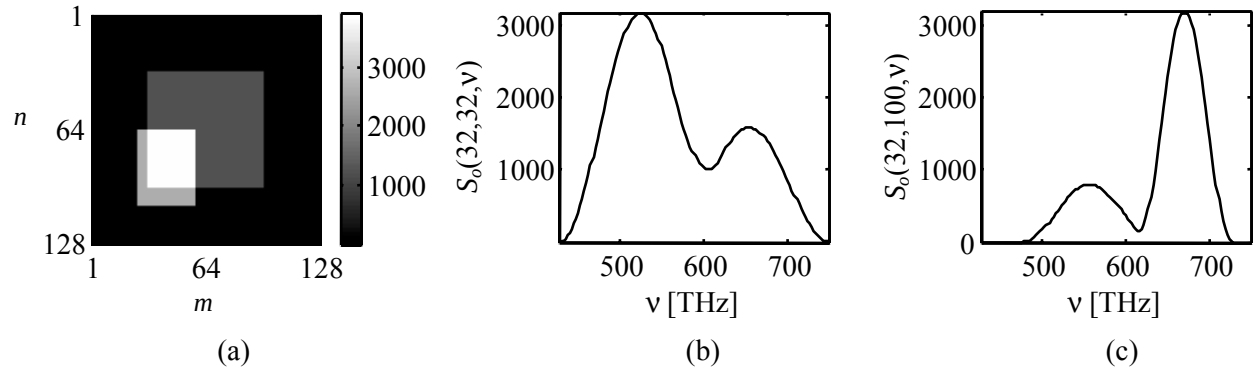

Figure 4. Object for the simulation: (a) spatial slice of the object spectral density at a particular optical frequency, (b) spectral density of the square object centered in the middle of the scene, and (c) spectral density of the rectangular object below and left of the center of the scene.

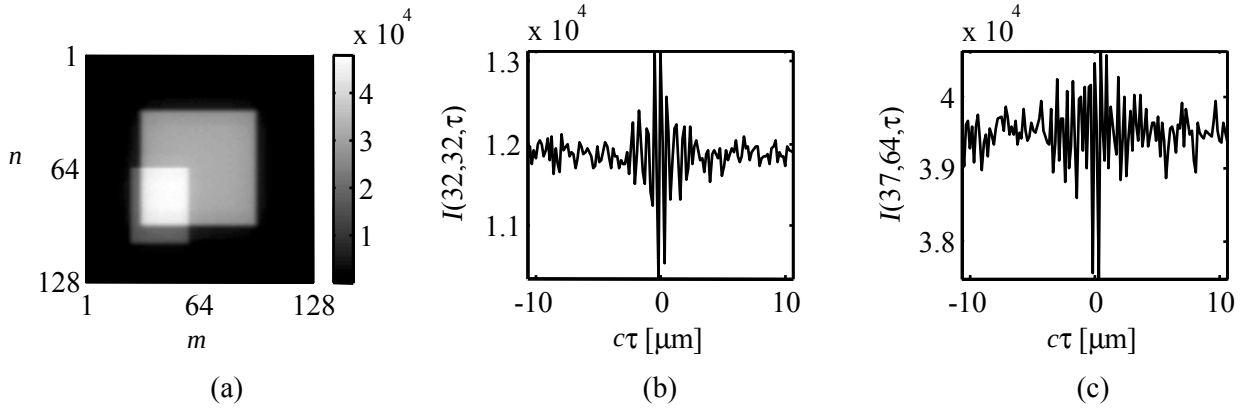

Figure 5. Simulation results for the raw data cube: (a) noisy image intensity at t = 0, (b) sampled fringe packet at $m = n = 32$, and (c) sampled fringe packet at $m = 37$ and $n = 64$.

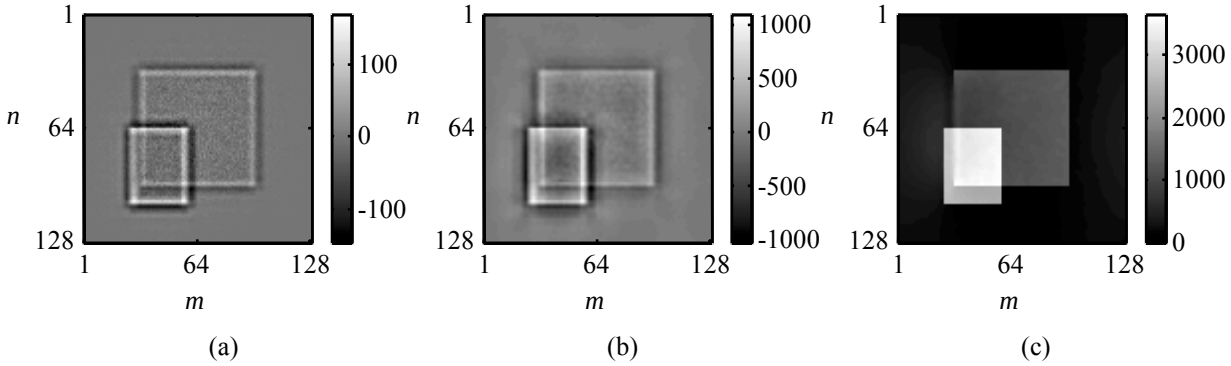

Figure 6. Simulation results for the spectral image at the same frequency as in Figure 4(a): (a) real part of data from the complex-valued spectral image cube (raw image), (b) Wiener-Helstrom filtered version of (a), and (c) results of nonlinear algorithm and DC restoration.

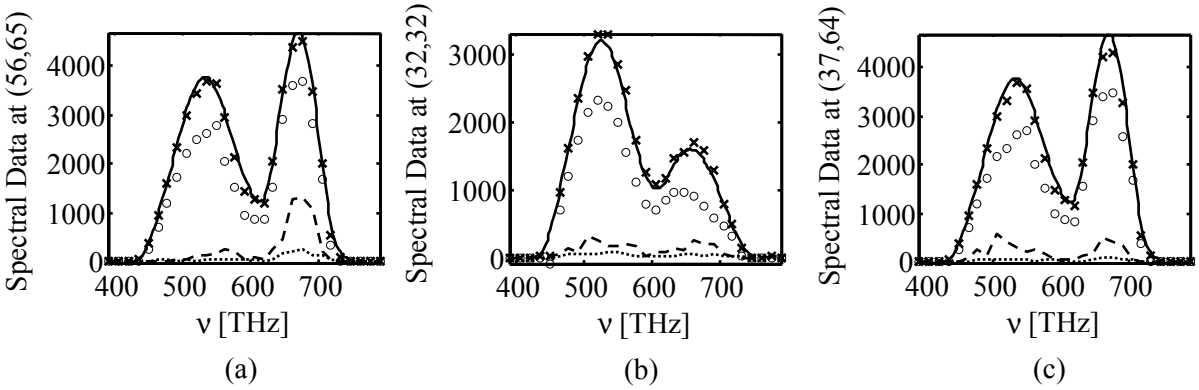

Figure 7. Spectral data at various spatial locations for: the object (solid lines), the real part of data from the complex-valued spectral image cube (dashed lines), the Wiener-Helstrom filtered data (dotted lines), and the reconstructed data using the nonlinear algorithm without the DC restoration (circles) and with the DC restoration (x's).

low spatial frequencies. Figure 6(c) shows one band of the band-by-band reconstruction results for maximizing Eq. (8) subject to the constraint that $C_l \geq 0$, and adding a DC component to make the reconstruction non negative. In this reconstruction, the normalization parameter σ_g for each band was chosen to be equal to 14% of the difference between the maximum and minimum values of the corresponding Wiener-filtered image. The initial guess for the optimization routine was the real part of the raw spectral image shown in Figure 6(a). As seen in Figure 6(c), the nonlinear algorithm has filled in the missing low spatial frequencies quite well.

Figure 7 shows spectral data at various spatial locations for: the object, the real part of the complex-valued spectral images, the Wiener filtered images, and the results of the nonlinear algorithm with and without the DC restoration. Figure 7(a) shows data for a point near an edge of one of the rectangles in the scene, while Figure 7(b) and 7(c) show spectral data for points that are not close to an edge. In each of the graphs, notice that the amplitude of the complex-valued raw spectral data is small compared to the object data, even in Figure 7(a), since the amplitude of the SOTF is small (maximum value = 0.33). The Wiener-Helstrom filter sharpens the spatial edges of the data, increasing the amplitude of the data near edges, but cannot reconstruct the data away from edges, due to the missing low spatial frequency data. The nonlinear algorithm does well at restoring all of the low spatial frequencies, except the DC components. Only after restoring the DC components does the reconstructed data agree well with the object data.

4. DISCUSSION

Fourier transform imaging spectroscopy can be performed with a segmented-aperture telescope or MTA by introducing path delays between various subapertures, using existing optical path length control mechanisms. Unlike the conventional optical transfer function, which is given by the autocorrelation of the entire pupil function for the telescope, the SOTF's for the resulting spectral images are given by the cross correlation between pupil functions for subaperture groups with different path delays. Since the subapertures do not physically overlap, these transfer functions vanish at the DC spatial frequency and are typically zero-valued in some finite area around DC. Thus, the resulting spectral images are missing low spatial frequency information, which cannot be restored by a linear reconstruction. We have shown that missing low spatial frequencies (except for DC) can be restored by maximizing a nonlinear sharpness metric involving the spatial derivatives of the object estimate. The DC components were restored by enforcing a non-negativity condition for the reconstruction on a band-by-band basis after maximizing the sharpness metric. Agreement between the reconstructed and the object data was best after the DC components were restored.

The use of the derivative-based sharpness metric implies a particular assumption about the scene, namely that it is composed of objects that are fairly uniform in the spatial dimensions. This is certainly true for the object data used in our simulation. We have had some success when applying the same algorithm to imagery of natural scenes. In

experimenting with the metric, we have found that the ability to successfully restore the missing low spatial frequencies is dependent on noise, the size of the area of missing spatial frequencies around DC, and the choice of the normalization constant σ_g. We have yet to quantify the sensitivities of the metric to these factors.

So far we have only reconstructed FTIS data on a band-by-band basis, starting with the recovered spectral images, which do not contain any low spatial frequency information. Improved performance can be expected by reconstructing the whole cube simultaneously. The raw intensity measurements contain polychromatic, low spatial-frequency information that is not in the recovered spectral images. Since this data is polychromatic, it can only be incorporated into the reconstruction as a constraint for the whole cube. In the simulation of Sec. 3, the total number of photons in any one intensity measurement is 1.64×10^8, whereas the total number of photons in the reconstructed cube is 1.94×10^8, which should be the same by energy conservation. When the whole cube is reconstructed simultaneously, additional constraints involving the polychromatic low spatial-frequency data and a non negativity condition should yield a more accurate reconstruction of the DC components and low spatial frequencies for each spectral band. Reconstructing the whole cube at once will have the additional benefit of deconvolving the data in the spectral dimension.

ACKNOWLEDGEMENTS

This work was supported by Lockheed Martin Space Systems Company.

REFERENCES

1. J. S. Fender, "Synthetic apertures: an overview," in *Synthetic Aperture Systems*, J. S. Fender, ed., Proc. SPIE **440**, 2-7 (1983).
2. S.-J. Chung, D. W. Miller, and O. L. de Weck, "Design and implementation of sparse aperture imaging systems," in *Highly Innovative Space Telescope Concepts*, H. A. MacEwen, ed., Proc. SPIE **4849**, 181-191 (2002).
3. R. G. Paxman, T. J. Schultz, and J. R. Fienup, "Joint estimation of object and aberrations by using phase diversity," J. Opt. Soc. Am. A **9**, 1072-1085 (1992).
4. R. L. Kendrick, A. L. Duncan, and R. Sigler, "Imaging Fizeau interferometer: experimental results," presented at Frontiers in Optics, Tucson, Arizona, 5-9 Oct. 2003.
5. J. Kauppinen and J. Partanen, *Fourier Transforms in Spectroscopy*, (Wiley-VCH, Berlin, 2001).
6. N. J. E. Johnson, "Spectral imaging with the Michelson interferometer," in *Infrared Imaging Systems Technology*, Proc. SPIE **226**, 2-9 (1980).
7. R. L. Kendrick, E. H. Smith, and A. L. Duncan, "Imaging Fourier transform spectrometry with a Fizeau interferometer," in *Interferometry in Space*, M. Shao, ed., Proc. SPIE 4852, 657-662 (2003).
8. S. T. Thurman, J. R. Fienup, and R. L. Kendrick, "Imaging Fourier transform spectroscopy with multi-aperture telescopes," presented at Frontiers in Optics, Tucson, Arizona, 5-9 Oct. 2003.
9. J. Goodman, *Introduction to Fourier Optics 2nd ed.*, (McGraw-Hill, New York, 1996).
10. C. W. Helstrom, "Image restoration by the method of least squares," J. Opt. Soc. Am. **57**, 297-303 (1967).
11. B. R. Frieden, "Restoring with maximum likelihood and maximum entropy," J. Opt. Soc. Am. **62**, 511-518 (1972).
12. W. H. Richardson, "Bayesian-based iterative method of image restoration," J. Opt. Soc. Am. **62**, 55-59 (1972).
13. L. B. Lucy, "An iterative technique for the rectification of observed distributions," Astron. J. **79**, 745-754 (1974).
14. R. A. Muller and A. Buffington, "Real-time correction of atmospherically degraded telescope images through image sharpening," J. Opt. Soc. Am. **64**, 1200-1210 (1974).
15. J. R. Fienup and J. J. Miller, "Aberration correction by maximizing generalized sharpness metrics," J. Opt. Soc. Am. A **20**, 609-620 (2003).
16. D. M. Ryan, "Penalty and barrier functions," in *Numerical Methods for Constrained Optimization*, P. E. Gill and W. Murray, eds., (Academic Press, New York, 1974).
17. E. Polak, *Computation Methods in Optimization*, (Academic Press, New York, 1971) Sec. 2.3.
18. W. H. Press, S. A. Teukolsky, W. T. Vetterling, and B. P. Flannery, *Numerical Recipes*, (Cambridge University Press, Cambridge, 1992) Ch. 10.